Lab on a Chip

COMMUNICATION

View Article Online
View Journal | View Issue

Cite this: *Lab Chip*, 2020, **20**, 1554

Received 20th January 2020,
Accepted 17th April 2020

DOI: 10.1039/d0lc00063a

rsc.li/loc

High-sensitivity microliter blood pressure sensors based on patterned micro-nanostructure arrays†

Nianzuo Yu,[a] Yongshun Liu,*[b] Bai Ji,[c] Shuli Wang,[a] Yunyun Chen,[c] Tianmeng Sun,[d] Junhu Zhang *[a] and Bai Yang[a]

Herein we present a micro-nanostructure integrated liquid pressure sensor, which features an ultra-high sensitivity of 16.71 mbar^{-1}, a low-pressure regime of 2 mbar, a trace sample volume of less than 1.3 μL and a visible display element. The measurable pressure ranges of the sensors include not only from micro-scale fluids to bulk liquids but also from hydraulic pressures to blood pressures, opening a window for liquid pressure sensing in lab-on-chip platforms, point-of-care diagnostics, and even robotics.

Pressure sensors are attractive for many applications, including electronic skins, wearable devices, healthcare monitors, microfluidics and robotics.[1] Although strain sensors have recently been a hot research topic,[2–5] liquid pressure sensor development is still in its infancy.[6,7] Traditional methods for measuring liquid pressure are based on the changing length of a liquid column, but the sensitivity and stability of such systems are far from enough.[8] Fiber-based hybrid and capillary-assisted sensing methods have achieved precise requirements of the intended applications, while the requirement of complicated auxiliary instruments still needs to be addressed.[9–11]

Owing to their superior properties, including small sample volume, low cost and good portability, microfluidics provide a promising option for producing miniaturized liquid pressure sensors.[12–18] To further simplify the fabrication procedure, elastomeric and compatible materials such as poly-(dimethylsiloxane) (PDMS) have been recently adopted into fluidic sensing systems.[15] Because of its flexibility under fluid pressurization, which can simulate a circulatory system including a four-chamber heart, PDMS integrated pressure sensors have been demonstrated in several recent reports.[16,17] However, experimental detection of local fluid pressure in typical microfluidic elements, such as valves, pumps and mixings, is still inconvenient. Additionally, oxygen sensitive luminescent sensors have been integrated into microfluidics to measure fluidic pressures inside a microchannel, and because liquid pressures could be screened by a fluorescence microscope, a matched characterization method is achieved.[18] Despite these pioneering works, it remains a challenge to develop highly sensitive sensors that can monitor not only fluidic pressure environments in microfluidics, but also liquid pressures of bulk chambers. In addition, the acquirement of pressure data for existing sensors typically requires intricate circuits and electronic boards, which significantly increases the metering cost and is not always suitable for application in commercial systems.

In this paper, a patterned microstripe-nanopillar array is employed in microfluidic systems to measure liquid pressures. The patterned structure acts as a burst microvalve in microchannels, and its sensing ability is based on the specific flow behavior of fluids moving through the microvalve array. The pressure registration of the liquid pressure sensor (LPS) can occur *in situ*, and is visible by the naked eye without any additional energy source inputs or intricate data acquisition circuits required. The sensor is miniaturized and portable, at less than 7 cm^2, and can be constructed by standard microfabrication technologies that are available in conventional research laboratories, including photo-lithography, wet etching and soft lithography. Notably, by adjusting the dimensions of the LPS, it can achieve an ultra-high sensitivity of 16.71 mbar^{-1}, a low-pressure regime of 2 mbar, and a trace sample loss volume of less than 1.3 μL. In addition, the LPS is demonstrated to function well, with slight adaptations, for common liquids within an ultra-wide surface tension range, enabling its application for

[a] *State Key Laboratory of Supramolecular Structure and Materials, College of Chemistry, Jilin University, 130012, P. R. China. E-mail: zjh@jlu.edu.cn*
[b] *State Key Laboratory of Applied Optics, Changchun Institute of Optics, Fine Mechanics and Physics (CIOMP), Chinese Academy of Sciences, 130033, P. R. China*
[c] *Department of Hepatobiliary and Pancreatic Surgery, The First Hospital, Jilin University, P. R. China*
[d] *Institute of Immunology, International Center of Future Science, The First Hospital, Jilin University, P. R. China*

† Electronic supplementary information (ESI) available. See DOI:10.1039/d0lc00063a

sensing environmental fluidic pressures in changing microchannels, detecting the central venous pressures (CVP), and diagnosing the morbidity of hypertension, hypotension and arterial thrombosis. Ultimately, this suggests new application opportunities in microfluidic pressure sensors, wearable health monitors, medical diagnosis and even emerging robotic technologies.

Results and discussion

Overview of the LPS

The LPS is composed of a primary fluidic microchannel, five trapezoidal metering microchannels, a substrate with hydrophobic microstripe-nanopillar array (MSNP), and a finger pressing gas chamber (Fig. 1a). When the fluidic microenvironment is pressurized, fluids can inject into the LPS from the inlet of the primary microchannel (Fig. 1b). The inlet pressure can then be measured based on the amount of MSNP grids that fluids flow through, within the five metering microchannels. The fluidic flow equation in the primary microchannel is described as:[19,20]

$$\Delta P_1 = \frac{\rho}{2} V^2 \left(f \frac{L}{D} + \sum K_L \right) \quad (1)$$

where ΔP_1 is the pressure drop of fluid in microchannels, f is the friction factor, ρ is the fluid density, V is the average velocity, L is the length of the microchannel, D is the diameter of microchannels, and $\sum K_L$ represents the sum of pressure loss due to the inlet and the varied dimensions of the microchannels. Theoretically, due to the pressure drop existence, the inner fluidic pressure should gradually decrease in the primary microchannel, and the fluidic pressure in the five metering microchannels should also decrease sequentially. There are burst microvalves with varied MSNP array lengths under the trapezoidal metering microchannels, and the burst pressure of the MSNP increases with decreasing length of the exposed structure. Therefore, the positions that the fluid fronts reach in the five metering microchannels differs, and the inlet pressure can be measured (Fig. 1c). To achieve repeated detection of liquid pressures, the outlets of the metering microchannels are connected to a gas pump. The fluids in the metering microchannels can be forced to return to the primary microchannel by pressing the gas chamber with a finger (Fig. 1d).

The MSNPs were fabricated using photo-lithography and reactive ion etching (RIE) to achieve the structure in Fig. 2a, then the structures were treated with trichloro(1*H*,1*H*,2*H*,2*H*-perfluorooctyl)silane (PFS). The advancing contact angles of the PFS-modified MSNPs and PDMS surfaces were 117.4 ± 0.9° and 123.0 ± 0.7°, respectively (Fig. S1a and b†). First, the single metering microchannel was compressed onto the MSNPs, and the flow behavior of water was investigated. As shown in Fig. 2b, as the fluidic inlet pressure was changed, the water fronts reached corresponding positions on the hydrophobic MSNP arrays. Experimentally-measured burst pressures increased with the decreasing length of the exposed MSNPs in the microchannels (Fig. 2g). The theoretical burst pressures in these microchannels could be calculated according to the Young–Laplace equation, which is described as[21–23]

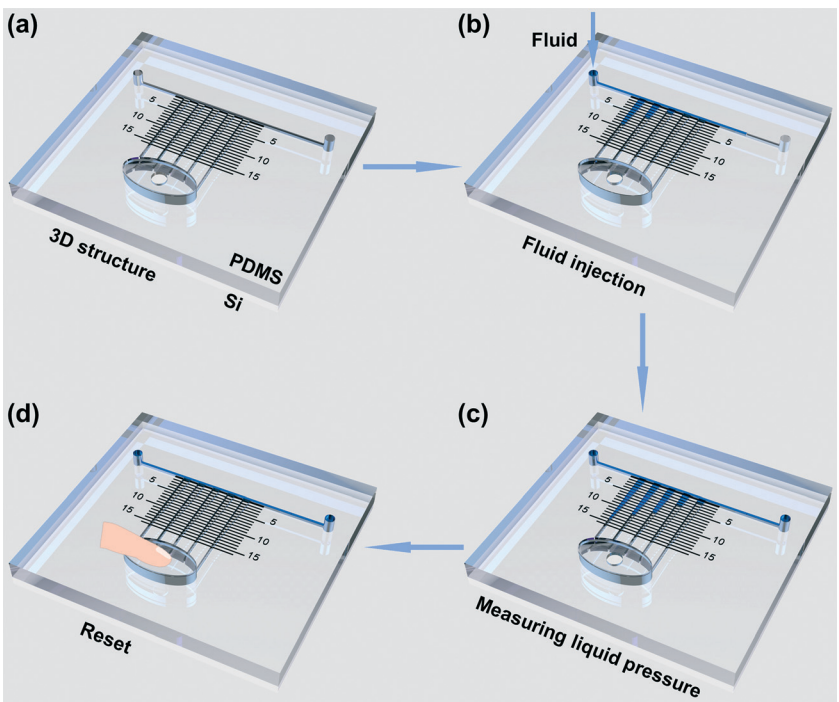

Fig. 1 (a–d) Schematic illustration of the LPS, showing (a) 3D structure of the LPS, (b) fluids flow within the LPS, (c) liquid pressures measured according to the quantity of grids filled by fluids, and (d) reuse of the LPS realized by pressing the gas chamber with a finger.

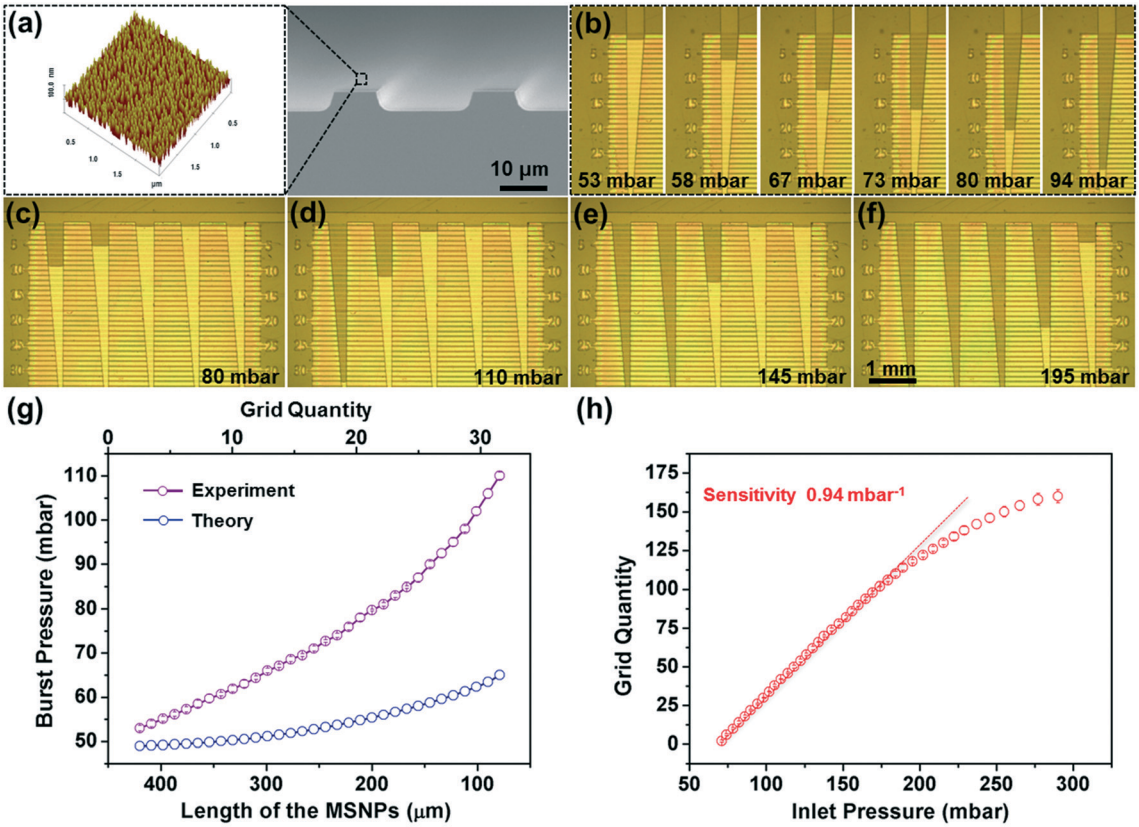

Fig. 2 (a) The morphology of the MSNP array surface, as evaluated by AFM and SEM. (b) Optical microscopy images of water that requires larger hydraulic pressure to enable flow through the narrower MSNP in a single metering microchannel. (c–f) Optical microscopy images of water filling more grids in the metering microchannels, corresponding to larger applied pressure in the liquid inlet. (g) Experimentally measured and theoretical bursting pressures as a function of the length of exposed MSNP in the single metering microchannel. (h) The amount of the grid that is filled with water as a function of the applied pressure of the liquid inlet. The figures in the images represent the applied pressure of the liquid inlet. Errors bars represent standard error.

$$\Delta P = P_I - P_O = -\sigma\left(2\frac{\cos\theta_S}{W} + \frac{\cos\theta_S}{H-h} + \frac{\cos\theta_V}{H-h}\right) \quad (2)$$

where P_I and P_O are the pressures inside and outside the liquids, respectively, W is the width of microchannel, H is the height of microchannel, h is the height of MSNP, σ is the surface tension of fluid, θ_V and θ_S are the advancing contact angles of fluids on the Si and PDMS surfaces, respectively. The pressure value and the growth trend of the measured pressures are both greater than those of the theoretical burst pressures. We believe the pressure value difference can be attributed to the pressure drop of fluids in the inlet, and the gradually increasing growth trend can be caused by the increased force area resulting from water flowing through new grids.[24]

As a standard fluidic pressure sensor, the device should be able to detect every change in inlet pressure, while fluids may not flow through a new MSNP in the single microchannel when we increase the inlet pressure by one unit (Fig. 2g). Therefore, five metering microchannels, which were embedded with MSNP arrays of varying lengths, were fabricated along the side of the primary fluidic microchannel. By properly designing the dimensions of the microchannels and the positions of the MSNPs (Fig. S1c and d†), the fluidic pressure change can be measured by the LPS with an increment unit of 1 mbar. When the inlet pressure was increased to 68.0 mbar, water started to fill the grid of the first flow metering microchannel. Water filled more grids as the inlet pressure was further increased (Fig. 2c–f, Video S1†), and there is a linear relationship between the quantity of grids in the five metering microchannels filled by water and the inlet pressure, within a certain pressure regime of 68–197 mbar (Fig. 2h). Furthermore, within this regime, each value of the inlet pressure corresponds to a single, special quantity of filled grids. When the inlet pressure is larger than 197.0 mbar, the linear relationship is no longer maintained (Fig. S2a–l†), but the deficiency can be overcome by using an increased quantity of metering microchannels (Fig. S2m–t†). While this increases the size of the LPS, and the specific quantity of the metering microchannels can be designed, as required, for each application. The sensitivity of an LPS is defined as $S = N/\Delta P_2$, where N is the quantity of grids filled by liquids and ΔP_2 is the variation of inlet pressures. The sensitivity of the proposed LPS used for water pressure sensing can reach a value of 0.94 mbar^{-1}.

Performance of the LPS

>For any LPS, performance properties including the measurement regime, sensitivity, stability, response time and applicability are important to characterize.

Measurement regime. When the inlet pressure was increased to 240.0 mbar, the aforementioned LPS was no longer accurate, as water flowed through the first metering microchannels. Because the energy barrier for fluids is increased in shallow microchannels, reducing the microchannel height is one potential strategy to increase the upper limit of the measurable pressure range (Fig. 3a and e and S3a–d†). Alternatively, metering microchannels with increased height, positioned close together, were fabricated to enable low pressure-range LPS (Fig. 3b, c and e and S3e–l†). Metering microchannels with more distant spacing exhibit large regimes in terms of the maximum measurable pressures, but the linear relationship between the measured pressure and the quantity of filled grid could be not established (Fig. 3d and e and S3m–p†). This result can be understood using eqn (1). When the spacing of the metering microchannels is distant, the values of L and ΔP_1 are large. When we gradually increased the inlet pressure, the quantity of filled grids may not increase in the 2nd, 3rd, 4th and 5th metering microchannels, but it will increase when we significantly increase the inlet pressure. This behavior produces a nonlinear increase in the total quantity of filled grids, which results in the nonlinear relationship. For reproducible experimental results, the measurement regime for water can be 2–800 mbar, and this range could be further enlarged by increasing the pressure loss in the liquid inlets (to increase the upper limit) and the microchannel height of LPS (to decrease the lower limit).

Sensitivity and stability. According to eqn (2), the difference of burst pressures on the MSNPs in high metering microchannels is small, improving the sensitivity of the LPS. Contrarily, the sensitivity of an LPS with shallow microchannels is relatively low (Fig. 3e). Positioning the metering microchannels more closely can reduce the ΔP_1 and increase the sensitivity simultaneously. The sensitivity of an LPS can be further enhanced by connecting the LPS with a narrow outlet and magnifying the dimension angle of the metering microchannels (Fig. S4†). Through these strategies, the sensitivity can reach 14.63 $mbar^{-1}$ for water, and the stability has been demonstrated through over 50 cycle experiments (Fig. S5a†).

Response time. To complete the grid filling in metering microchannels, fluids must flow through the primary microchannel and the MSNP arrays in the metering microchannels. In our experiments, fluids are pressure-driven, and the fluid flow rate is related to the inlet pressure. Therefore, the time that it took for fluids to flow through the

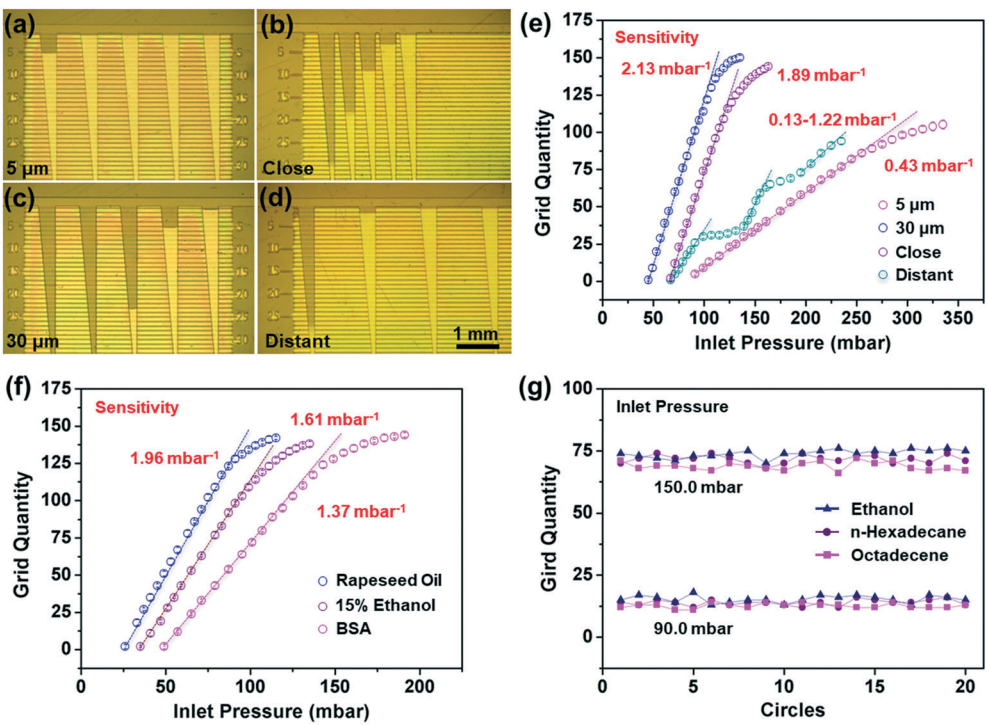

Fig. 3 (a–d) Optical microscopy images of metering microchannels with heights of (a) 5 and (c) 30 μm. The applied pressure of liquid inlet is 90.0 mbar. (e) The corresponding relationship between the quantity of grids filled by water and the applied pressure of the liquid inlet, for different microchannel dimensions. (f) The corresponding relationships between the quantity of grids filled with fluid and the applied pressure of liquids with a wide surface tension range and multiphase liquids. (g) The stability of LPS with an integrated reservoir for multiple liquids with extremely low surface tensions. The surface tensions of the BSA solution, 15% ethanol, rapeseed oil, *n*-hexadecane, alcohol, and octadecene are 52.5, 44.3, 31.6, 25.2, 22.1, and 22.0 mN m^{-1}, respectively. The microchannel height of the LPS is 10 μm.

primary microchannel and MSNP array decreases with increased measured pressure (Fig. S5b†). When the inlet pressure is 130.0 mbar, the response time is 6.3 ± 0.5 s (Video S1†). The dimensions of the LPS also influence the response time. We found that high metering microchannels produced shorter response times than shallow microchannels at the same measured pressure, because the lower energy barrier in the high microchannel enabled a larger flow rate.

Applicability. The materials of the LPS include a PDMS microchannel and a structured Si-MSNP surface, and the fabrication procedures involve standard photo-lithography and wet etching, which are straightforward and cost-effective compared to the fabrication procedures required for current LPS.[13,14] To enable the grid quantity to be easily quantified, we added a ruler line to the side of the MSNP array. More importantly, current LPS require sophisticated optical and electronic data displays and acquisition equipments,[4–6] while the proposed LPS can be utilized *in situ*, is visible by the naked eye, and is recordable by a typical cell phone camera. The consumed liquids during the measurement process include the liquid in the LPS and the liquid connecting the LPS and the pressure chamber, and can be calculated according to the dimensions of the microchannel and the area of filled fluids. The volume is notably low, at less than 1.3 μL, so the produced LPS can provide an option for liquid pressure in sample-limited applications (Fig. S5c†).

Pressure sensing for liquids with low surface tension

To demonstrate the applicability of the proposed LPS for traditional microfluidics systems, we measured its pressurized measurement ability for liquids with low surface tension, including both oil phase and water phase liquids (Fig. S6†). It is worth mentioning that the relationship between inlet pressure and the quantity of filled grids varies is related to the surface tension of liquids. According to eqn (1) and (2), the metering regime of the LPS for liquids with lower surface tension values is smaller, in contrast to the trend for sensitivity (Fig. 3f). As for the liquids with extremely low surface tension such as alcohol, *n*-hexadecane and octadecene, the $\cos\theta_V$ and $\cos\theta_S$ of these liquids are positive values, while the ΔP is negative. The energy barrier of the MSNP array could not affect the fluid flow, so fluids will freely flow through the entire of the microchannel system. Therefore, the present metering method lost its sensing ability, and new devices had to be fabricated. A reservoir was included between the inlet and the metering microchannels (Fig. S7a and b†), and we filled the reservoir and the fluidic microchannel with water using a low inlet pressure so that no fluid could flow into the metering microchannels. Low surface tension liquids can then be subsequently injected from the inlet, and the measurement process will be completed before the low surface-tension liquids can flow through and diffuse into the metering microchannels (Fig. S7c–e†). Based on the measurement results for the liquids with extremely low surface tension (Fig. 3g), we believe the LPS with an integrated reservoir can measure the fluidic pressure of liquids with low surface tensions, as long as the liquid does not react with the chip materials. In addition, the reservoir integrated LPS also suitable for measuring of liquids with unknown surface tension, because the measurement capability and the resulting values are independent of the surface tension of the liquids.

Detecting the environmental pressure of fluids in microchannels

In typical microfluidic chips, changes in the diameter and shape of fluidic microchannel are a common result of connecting to other chip elements, so it is crucial to understand the effect of this on the fluidic pressure.[22,23] However, theoretically calculated equations describing these changes of environmental fluid pressure in microchannels are currently incomplete, and typical experimental detection of local fluid pressure in microchannels sidewall is inconvenient and cost-consuming.[24] The LPS proposed here can provide a new strategy for solving this problem. To simulate various fluid microenvironments, we fabricated primary microchannels with round, triangular, and square physical structures serving as obstacles to flow, and the filling behaviors of water were investigated. As shown in Fig. 4a–d, the number of filled grids was gradually reduced, so we can obtain the increased fluidic pressure drop, from 32.07 to 55.28 mbar (Fig. 4m), according to the relationship in Fig. 2g and h. The results demonstrate that the energy barrier of the three kinds of obstacles gradually increases and overcomes that of the straight microchannel.

The primary microchannels were fabricated with varied widths to determine the influence of microchannel diameter on fluidic pressure. The results indicate that the pressure difference between the metering microchannels is greater for narrower fluidic microchannels (Fig. S8†). According to eqn (1), a narrower microchannel corresponds to a larger pressure drop, and the quantity of filled grids would vary more significantly among the five metering microchannels. To study the fluidic pressure changes in microchannels where the diameter is changed suddenly, LPSs were fabricated with variations in the primary microchannels produced. As shown in Fig. 4e–h, microchannels with wider spacing correspond to larger energy barriers in junctions, which subsequently increases the pressure drop in the primary microchannel from 31.93 to 53.31 mbar (Fig. 4n). Simultaneously, we experimentally determined that the pressure drop in narrower contractive microchannels is larger than that in wider microchannels (Fig. 4i–l and n), which is consistent with the theoretical prediction of eqn (1). In addition, the inner fluidic pressure in different microchannel chambers was measured (Fig. 4e–l). We found that as the primary microchannel gradually widened, the internal fluid pressure remained consistent, and the same conclusion is established in primary microchannels with both the outspread and contractive outlets (Fig. 4o).

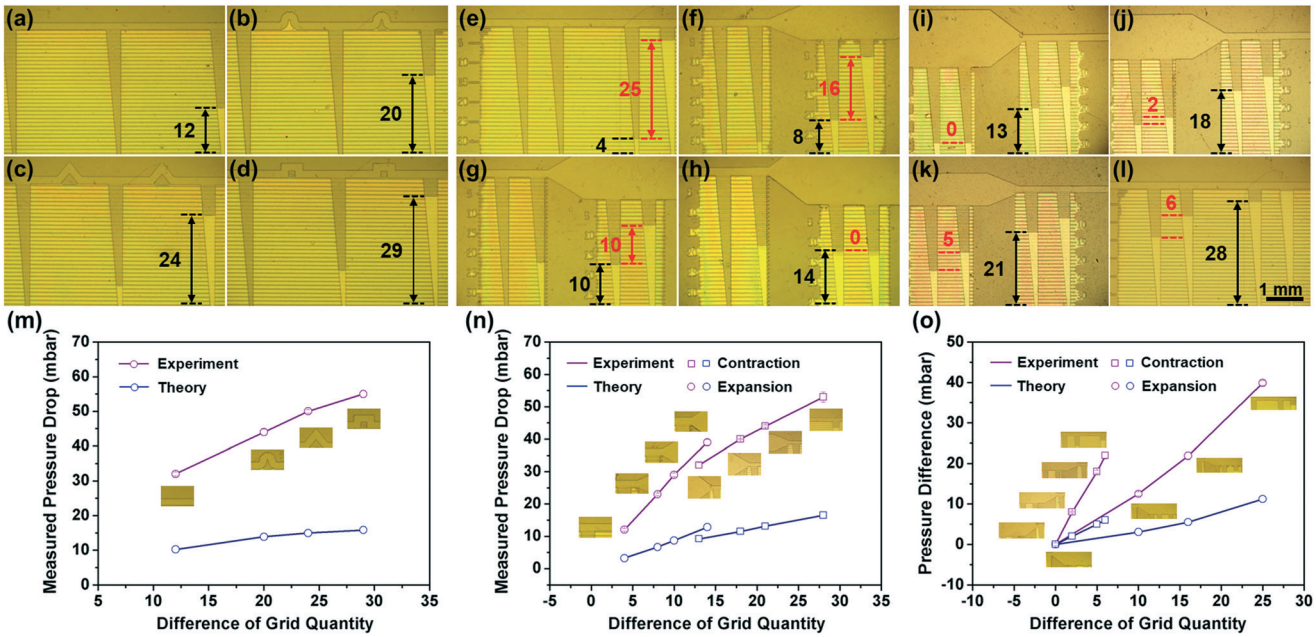

Fig. 4 (a) The filling behavior of water in the metering microchannels with distant spacing. (b–d) The filling behavior of water in the LPS when the straight fluidic microchannels are integrated with rounded (b), triangular (c) and square (d) obstacles, respectively. The line lengths of the fluidic microchannels are identical in (a–d), and the applied pressure of the liquid inlet is 200.0 mbar. (e–l) The filling behavior of water in the LPS with microchannels that is suddenly widened and narrowed. The microchannel heights of the LPS are 10 μm. Black arrows and labels represent the pressure drop in the metering microchannels, and red arrows and labels represent the difference of the inner fluidic pressure among the metering microchannels. The applied pressure of the liquid inlet is 180.0 mbar (e–h), or 130.0 mbar (i–l). (m and n) Experimentally measured and theoretical pressure drops as a function of the difference in the number of grids filled with fluid in different microchannels. (o) Experimentally measured and theoretical environmental pressure difference in the number of grids filled with fluid in both widened and narrowed microchannels.

Detecting the central venous pressure and diagnosing the severity of hypertension, hypotension, and arterial thrombosis of rats

Sensing of the CVP contributes to the measurement of effective circulating blood volume and cardiac function.[25–27] However, current metering methods require a significant volume of blood to fill a liquid column, and the accuracy suffers from multiple uncertainties, such as residual air bubbles in measuring columns.[28] The proposed LPS provides a promising alternative, due to its high sensitivity and small sample volume requirement (Fig. 5a). To demonstrate this, we first connected the LPS to a closed pressurized blood chamber to simulate a venous pressure environment and obtain the flow law for rat blood in the LPS. The sensitivity of the LPS for blood in this environment was found to be 16.71 $mbar^{-1}$ (Fig. 5b and Fig. S9a–c†). It is worth mentioning that the metering ability of the LPS is related to the surface tension of liquid, and the law is also suitable for the pressure measurement of other types of blood, such as bovine blood (Fig. S10†). We then connected the LPS to the proximal cerebral end of the right external jugular vein of three groups of rats (all of the experimental animals in this study were treated in accordance with protocols approved by the Institutional Animal Care and Use Committee of Jilin University, Changchun, People's Republic of China):[29] (1) an untreated control group, (2) rats that were intravenously injected with 2 mL kg^{-1} 0.9% saline, and (3) rats that were intravenously injected with 0.8 μg kg^{-1}. As shown in Fig. 5c–e, the rats having a low blood volume could be diagnosed according to the quantity of grids filled by the bloods.

Direct detection of arterial blood pressure is the "gold standard" for obtaining absolute blood pressure, which avoids interference from external factors that impact traditional and wearable monitoring devices.[30] To ensure that the measurement range of the LPS is wide enough to detect both hypertension and hypotension in rats, the microchannel height of LPS was chosen to be 5 μm, with a corresponding sensitivity of 1.37 $mbar^{-1}$ (Fig. 5f and S9d–f†). Then, the LPS was connected to the left carotid artery of rats by a puncturing method,[31] and adrenaline and acetyl choline were used to control the arterial blood pressure of the rats. As shown in Fig. 5g–i, the LPS can detect the systolic blood pressure of rats, and the severity of hypertension and hypotension can be diagnosed according to the quantity of the grids filled by bloods (Video S2†).

In addition, arterial thrombosis is a main instigating factor of heart attacks and strokes,[32] so convenient detection for arterial thrombosis by a low-cost device could reduce the incidence of these diseases. To simulate the conditions of arterial thrombosis, we clipped the common carotid artery of rats with varied force.[33] We found that the quantity of girds filled by blood decreased with increasing clipping (Fig. 5j–l), demonstrating the monitoring ability of the LPS for the severity of arterial thrombosis.

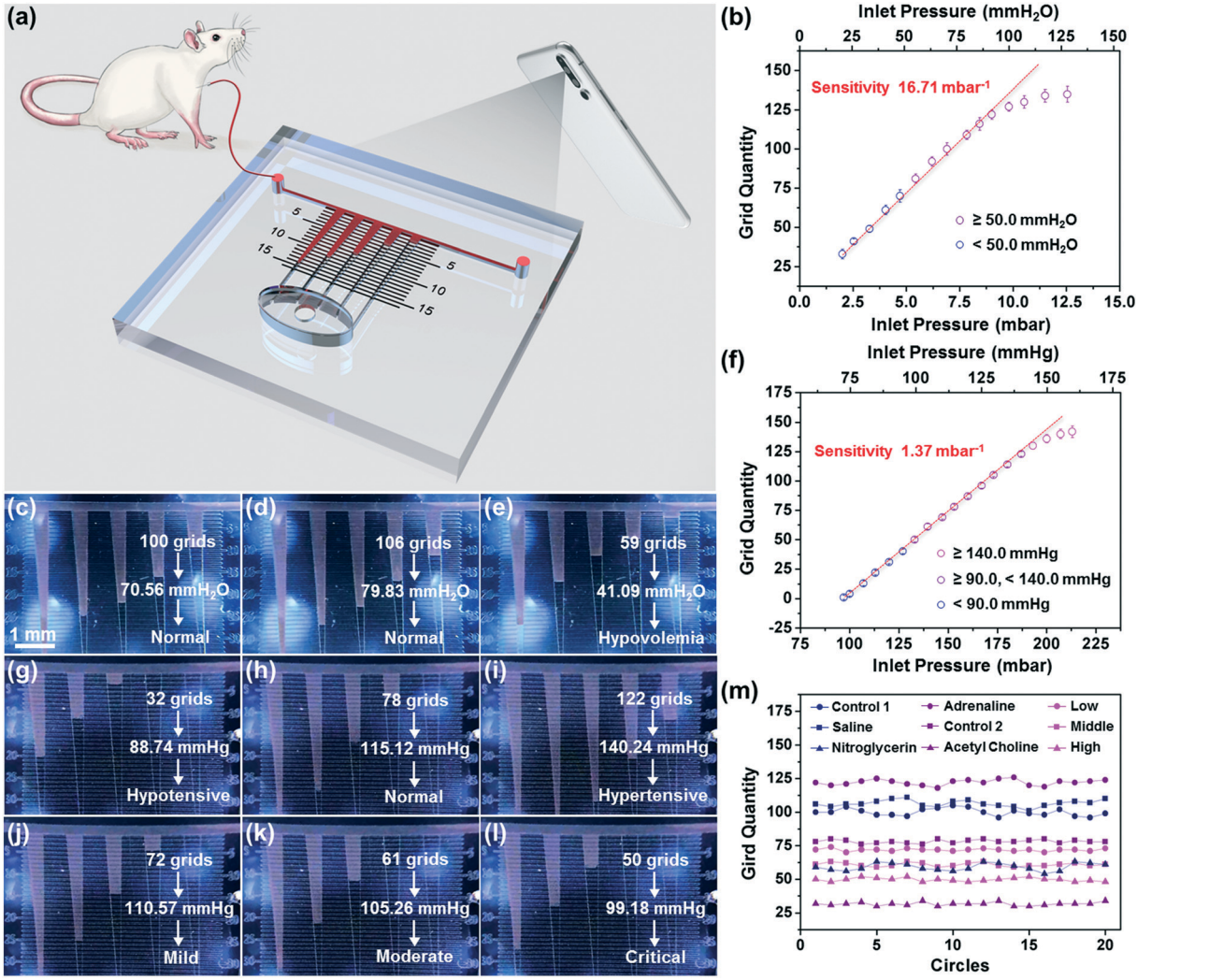

Fig. 5 (a) Schematic of the LPS for monitoring the blood pressure of rats. (b) The corresponding relationships between the quantity of grids filled with blood and the applied pressure of the simulated CVP. The microchannel height of the LPS is 83 μm. (c–e) The LPS for sensing the CVP of rats, which is imaged with a typical built-in cell phone camera. The rats in (c) were untreated as a control, and the rats in (d) and (e) were intravenously injected with 2 mL kg^{-1} 0.9% saline and 0.8 μg kg^{-1} nitroglycerin, respectively. (f) The corresponding relationships between the quantity of grids filled with blood and the applied pressure of the simulated blood chamber. The microchannel height is 5 μm. (g–i) The LPS for measuring the severity of hypertension and hypotension. The rats in (h) were untreated as a control, and the rats in (g) and (i) were intravenously injected with 0.2 mL kg^{-1} 0.01% adrenaline and 0.2 mL kg^{-1} 0.01% acetyl choline, respectively. (j–l) The LPS for diagnosing arterial thrombosis of rats, where the common carotid artery of the rats was clipped with low (j), middle (k) and high (l) pressures. (m) The reproducibility measurement results for the LPS used to detect the CVP and the severity of hypertension, hypotension, and arterial thrombosis.

All the measured results discussed above were repeated, as shown in Fig. 5m. It is noteworthy that the blood pressure can be measured *in situ* and recorded by a typical built-in cell phone camera, without the requirement for additional energy sources, suggesting the LPS could provide great portability, with a floor space less than 7 cm^2. In addition, the loss of blood volume is less than 1.3 μL, which is much lower than that required for current clinical methods and would not affect patient health, even in a clinical emergency.[28]

Conclusions

In conclusion, a visualized and highly sensitive LPS has been constructed using an integrated micro-nanostructure array in microchannels, providing a powerful strategy for developing a miniaturized, portable LPS. Notably, the LPS features an adjustable pressure regime reaching as low as 2 mbar, an ultra-high sensitivity of 16.71 $mbar^{-1}$, a low sample volume of less than 1.3 μL and a convenient display element that can be instantaneously visualized *in situ* by the naked eye without the need for intricate data acquisition circuits or extra energy source inputs, enabling sensing of common liquids with an ultra-wide range of surface tensions. In addition, the LPS is suitable for detecting not only the fluid pressure in a microfluidic system and bulk chamber, but also the blood pressure in the arteries and veins of rats. By integrating the LPS with curving, contractive and outspread microchannels, we could experimentally determine the fluidic environment

pressure of target positions in microfluidic systems, which is difficult to realize using traditional pressure sensors. The LPS appears to be a highly sensitive monitor to measure the value of the CVP, along with the severity of hypertension, hypotension, and arterial thrombosis. Further, the LPS is miniaturized and portable, and thus can be carried around and used for testing in a variety of environments and applications.

The obtained results offer compelling evidence in favor of this newly designed LPS, providing a new alternative for liquid pressure measuring in applications including lab-on-chip platforms, chemical engineering, point-of-care diagnostics, robotics, and beyond. Further investigations can be conducted to achieve a pneumatic and pressure-tight LPS platform that will allow non-invasive blood pressure measurement by sensing the arterial pulse. A platform may also be constructed by flexible substrate materials to yield low profile and wearable configuration that can be portable and easily deployed.

Conflicts of interest

The authors declare no conflicts.

Acknowledgements

This work was supported by the National Natural Science Foundation of China (grant no. 21774043, 21975098 and 61727813), the Fundamental Research Funds for the Central Universities (JLU) and JLUSTIRT (2017TD-06), the 2018 Ph.D. Interdisciplinary Research Grant (10183201818).

Notes and references

1 D.-H. Kim, N. Lu, R. Ma, Y.-S. Kim, R.-H. Kim, S. Wang, J. Wu, S. M. Won, H. Tao, A. Islam, K. J. Yu, T.-i. Kim, R. Chowdhury, M. Ying, L. Xu, M. Li, H.-J. Chung, H. Keum, M. McCormick, P. Liu, Y.-W. Zhang, F. G. Omenetto, Y. Huang, T. Coleman and J. A. Rogers, *Science*, 2011, **333**, 838–843.
2 S. C. B. Mannsfeld, B. C. K. Tee, R. M. Stoltenberg, C. V. H. H. Chen, S. Barman, B. V. O. Muir, A. N. Sokolov, C. Reese and Z. Bao, *Nat. Mater.*, 2010, **9**, 859–864.
3 P. M. Valencia, E. M. Pridgen, M. Rhee, R. Langer, O. C. Farokhzad and R. Karnik, *ACS Nano*, 2013, **7**, 10671–10680.
4 R. Li, B. Nie, P. Digiglio and T. Pan, *Adv. Funct. Mater.*, 2014, **24**, 6195–6203.
5 X. Li, M.-H. Yeh, Z.-H. Lin, H. Guo, P.-K. Yang, J. Wang, S. Wang, R. Yu, T. Zhang and Z. L. Wang, *ACS Nano*, 2015, **9**, 11056–11063.
6 B. Nie, R. Li, J. Cao, J. D. Brandt and T. Pan, *Adv. Mater.*, 2015, **27**, 6055–6062.
7 B. H. Son, J.-Y. Park, S. Lee and Y. H. Ahn, *Nanoscale*, 2015, **7**, 15421–15426.
8 N. Srivastava and M. A. Burns, *Lab Chip*, 2007, **7**, 633–637.
9 C.-S. Kim, B. K. Kang, J. H. Jung, M. J. Lee, H. B. Kim, S. S. Oh, S. H. Jang, H. J. Lee, H. Kastuyoshi and J. K. Shin, *Jpn. J. Appl. Phys.*, 2010, **49**, 03CC03.
10 C. Pan, Z. Li, W. Guo, J. Zhu and Z. L. Wang, *Angew. Chem., Int. Ed.*, 2011, **50**, 11192–11196.
11 Y. Chen, H. N. Chan, S. A. Michael, Y. Shen, Y. Chen, Q. Tian, L. Huang and H. Wu, *Lab Chip*, 2017, **17**, 653–662.
12 G. M. Whitesides, *Nature*, 2006, **442**, 368–373.
13 J. Chen, H. Guo, J. Zheng, Y. Huang, G. Liu, C. Hu and Z. L. Wang, *ACS Nano*, 2016, **10**, 8104–8112.
14 X. Zhang, Y. Zheng, D. Wang and F. Zhou, *Nano Energy*, 2017, **40**, 95–106.
15 A. Orth, E. Schonbrun and K. B. Crozier, *Lab Chip*, 2011, **11**, 3810–3815.
16 T. Jung and S. Yang, *Sensors*, 2015, **15**, 11823–11835.
17 W. Wu, X. Cao, J. Zou, Y. Ma, X. Wu, C. Sun, M. Li, N. Wang, Z. Wang and L. Zhang, *Adv. Funct. Mater.*, 2018, **29**, 1806331.
18 C. Hoera, A. Kiontke, M. Pahl and D. Belder, *Sens. Actuators, B*, 2018, **255**, 2407–2415.
19 M. Kundu, K. Vamsee and D. Maiti, *Asia-Pac. J. Chem. Eng.*, 2009, **4**, 450–461.
20 S. Molla, D. Eskin and F. Mostowfi, *Lab Chip*, 2011, **11**, 1968–1978.
21 N. Yu, S. Wang, Y. Liu, P. Xue, P. Ge, J. Nan, S. Ye, W. Liu, J. Zhang and B. Yang, *Langmuir*, 2017, **33**, 494–502.
22 S. Wang, N. Yu, T. Wang, P. Ge, S. Ye, P. Xue, W. Liu, H. Shen, J. Zhang and B. Yang, *ACS Appl. Mater. Interfaces*, 2016, **8**, 13094–13103.
23 N. Yu, S. Wang, H. Liu, P. Ge, J. Nan, S. Ye, J. Zhang and B. Yang, *Sens. Actuators, B*, 2018, **256**, 735–743.
24 W. L. Qu and I. Mudawar, *Int. J. Heat Mass Transfer*, 2002, **45**, 2549–2565.
25 L. Massicotte, S. Lenis, L. Thibeault, M. P. Sassine, R. F. Seal and A. Roy, *Liver Transplant.*, 2006, **12**, 117–123.
26 K. Damman, V. M. van Deursen, G. Navis, A. A. Voors, D. J. van Veldhuisen and H. L. Hillege, *J. Am. Coll. Cardiol.*, 2009, **53**, 582–588.
27 T. G. Eskesen, M. Wetterslev and A. Perner, *Intensive Care Med.*, 2016, **42**, 324–332.
28 E. M. Dunki-Jacobs, P. Philips, C. R. Scoggins, K. M. McMasters and R. C. G. Martin, *Ann. Surg. Oncol.*, 2014, **21**, 473–478.
29 D. A. Berlin and J. Bakker, *Crit. Care*, 2015, **19**, 324–332.
30 E. Chung, G. Chen, B. Alexander and M. Cannesson, *Front. Med*, 2013, **7**, 91–101.
31 X. B. Ona, L. M. Garcia, I. Sola and X. B. Cosp, *Cochrane Database Syst. Rev.*, 2011, **7**, CD007887.
32 P. F. Costa, H. J. Albers, J. E. A. Linssen, H. H. T. Middelkamp, L. van der Hout, R. Passier, A. van den Berg, J. Malda and A. D. van der Meer, *Lab Chip*, 2017, **17**, 2785–2792.
33 D. Tsuchiya, S. Hong, T. Kayama, S. S. Panter and P. R. Weinstein, *Brain Res.*, 2003, **970**, 131–139.